aDOI: 10.1002/ ((please add manuscript number))
Article type: Full Paper

Regulation on Lamellar Structure of Vanadium Oxide via Polyaniline Intercalation for High-Performance Aqueous Zinc-ion Battery

*Song Chen, Kang Li, Kwan San Hui and Jintao Zhang**

S. Chen, Prof. Dr. J. Zhang
Key Laboratory for Colloid and Interface Chemistry, Ministry of Education
School of Chemistry and Chemical Engineering
Shandong University, Jinan 250100, China
E-mail: jtzhang@sdu.edu.cn

Dr. K. S. Hui
School of Engineering
University of East Anglia, Norwich NR4 7TJ, United Kingdom

Abstract: According to the intercalation mechanism, a proper modulation on channel structures of metal oxides is crucial to reversibly accumulate large zinc ions with high surface charge density for improving aqueous zinc-ion battery performance. However, the irreversible structure-transition commonly results in serious capacity decay and low specific capacity. Herein, polyanilines are in-situ intercalated into the layered vanadium oxide in order to enlarge the lamellar spacing for enhancing the zinc-ion battery performance. With enlarged lattice spacing, the polyaniline intercalated vanadium oxide coupled with a Zn electrode exhibited a large specific capacity of 372 mAh g^{-1} and good cycling stability. More importantly, in-situ characterization results revealed that the polyaniline intercalated vanadium oxide allows the accumulation of additional zinc ions without obvious phase transformation and the conjugated polymeric chains enable the structure flexibility in the confined layer space to relieve the intercalation stress for improving cycling stability. Additionally, findings from the in-situ infrared spectroscopy measurements elucidated the charge storage mechanism of the battery. Reversible doping processes of PANI molecules in vanadium oxide allow the involvement of multiple ions in the charge storage process, improving battery performance. Uncovering the origin of improved charge storage mechanism is of importance in rationally designing advanced materials with unique organic and inorganic features for high-performance aqueous zinc-ion batteries.

1. Introduction

Lithium-ion batteries (LIBs) has made significant achievements for energy storage and portable applications.[1-3] Along with sharply increasing demands on high-performance energy devices, it's an urgent requirement to design alternative batteries with better safety and large energy density. With an aqueous electrolyte, the metallic Zn has been coupled with intercalation compounds to fabricate safe and high-performance zinc-ion batteries (ZIBs).[4-7] Notably, the aqueous electrolyte with good ion-transfer ability is able to eliminate the safety issues caused by organic electrolytes. With a low redox potential (-0.76 V versus standard hydrogen electrode (SHE)), the metallic zinc can provide a high theoretical capacity of 820 mAh g^{-1} via the two-electron redox process.[8] Therefore, the aqueous ZIBs are highly promising alternative energy storage devices for future applications.[9]

Alkaline zinc-manganese primary batteries have been commercially used for a long time.[10, 11] However, the recent research efforts have been made to fabricate rechargeable high-performance ZIBs via rational designs of electrode materials, a better understanding of energy storage mechanisms and optimizations of electrolytes.[12] Typically, manganese oxides, Prussian blue analogues, vanadium-based oxides, and other intercalation compounds are used as the cathode of aqueous ZIBs.[13, 14] However, polymorph manganese oxides often exhibit poor cycling stability due to the phase transformation, whereas the specific capacity of Prussian blue analogues is relatively low owing to the narrow ion channel and poor electrical conductivity. Vanadium-based oxides with relatively good stability and fairly large capacity have been the focus of current research on aqueous ZIBs due to the layered structure.[15, 16] According to the traditional ion insertion/extraction mechanism, the large lattice channels are the basic requirement to reversibly accumulate large Zn^{2+} ions for the energy storage process.[17] H^+ ions are proposed to be involved in the energy storage process, enhancing the specific capacity of aqueous ZIBs.[18] Additionally, the structure collapse caused by irreversible structure transitions is a pressing challenge for improving cycling stability of electrode

materials. Recently, the polyaniline cathode delivered a long cycling life up to 3000 cycles on the basis of the reversible redox conversion reactions, but the specific capacity is lower than 100 mAh g^{-1}.[19] Notably, the intercalation of conductive polyaniline in the mesostructured vanadium oxide has been extensively investigated due to unique ion- and charge-transport characteristics.[20] Especially, the intercalation of PANI chains into vanadium oxide was demonstrated to expand the mesopores and enhance the electrical conductivity of the resultant nanocomposite,[21] which would enhance the batteries' performance. Unfortunately, to our best knowledge, the polyaniline intercalated vanadium oxide with a unique layer structure has not been reported for high-performance ZIBs. That requires a deeper understanding of the energy-storage mechanism.

Herein, the in-situ intercalation process was demonstrated to regulate the interlaminar space of layered vanadium oxide (V_2O_5) by intercalating polyaniline as guest materials. Specifically, the redox reaction between V_2O_5 and aniline monomers enabled the gradual intercalation of polyaniline chains among the interlaminar spaces of vanadium oxide with mixed valences. The intercalated structure was optimized by adjusting the ratio between vanadium oxide and aniline monomers in order to reversibly accumulate zinc ions. Thus, the aqueous ZIB exhibited a high specific capacity of 372 mAh g^{-1} at a current density of 0.5 A g^{-1}, superior to the recently reported results.[22, 23] More importantly, the reversible storage mechanism for the ZIB in the intercalated V_2O_5 with polyaniline was elucidated for the first time through findings from in-situ X-ray diffraction and in-situ infrared spectroscopy. A better understanding of the intercalation mechanism with polyaniline as the guest material is of importance in correlating the structure and composition information of intercalative materials with the electrochemical performance of ZIBs, providing general principles for the rational design of advanced electrode materials via the intercalation chemistry.

2. Results and discussion

2.1. Characterizations

As demonstrated in Figure 1a, the in-situ intercalation of vanadium oxide was achieved via a one-pot hydrothermal method (see Experimental Section). XRD analysis was performed to verify the successful intercalation of polyaniline into the layers of V_2O_5 (Figures 1b & S1). In comparison with the multiple diffraction peaks of the orthorhombic V_2O_5 precursor (JCPDS Card no. 41-1426), a large proportion of diffraction peaks disappeared after the hydrothermal treatment. Notably, the strongest peak for the (001) plane of V_2O_5 is shifted from 20.3 to 6.2°, suggesting the increasing lattice spacing. The calculated interlayer distance is about 1.42 nm, much larger than that of the original V_2O_5 precursor (~0.44 nm, Figure S2d), which would be contributed to the intercalation of polyaniline. The recent studies have revealed that the lattice spacing of vanadium oxides can also be enlarged by introducing the structural water and/or the interaction of Zn^{2+} ions along with water molecules.[15, 24] Typically, the lattice spacing of vanadium oxides is up to 1.26, 1.29 nm via the introduction of structural water ($V_2O_5 \cdot nH_2O$/graphene), the intercalation of Zn^{2+} ions and water ($Zn_{0.25}V_2O_5 \cdot nH_2O$), respectively. The introduction of water into vanadium oxides prepared via the hydrothermal method can not be avoided, which even can be achieved by the simple immersion into an aqueous electrolyte.[15] Nevertheless, the lattice spacing of the vanadium oxide intercalated with polyaniline and partial water in the present work is as large as 1.42 nm, which is the largest one, to the best of our knowledge. Therefore, the large lamellar structure would be attributed mainly to the interaction of polyaniline. Scanning electron microscopy (SEM) and transmission electron microscopy (TEM) were performed to investigate the morphology of the intercalated V_2O_5 sample prepared in the presence of 100 μL aniline monomers (PANI100-V_2O_5). In comparison with the vanadium oxide nanoparticles (Figure S2), the SEM images (Figures 1c & d) exhibit the uniform flakes with a thickness of around 8-10 nm. These nanosheets are interconnected each other to form the urchin-like structure. TEM images (Figures 1 e & f) show the thin-layer nature of nanosheets. High-resolution transmission electron microscopy (HRTEM) was employed to further characterize the interplanar spacing of (001) and the d-

spacing is measured to be around 1.43 nm, in good agreement with the XRD results, suggesting the presence of guest materials. According to FTIR spectra (Figure 1h), the characteristic bands at 495 and 621 cm^{-1} are attributed to the symmetric and asymmetric stretching modes of V-O-V in V_2O_5 precursor. The absorption peak at 833 cm^{-1} is related to the vibration of O-$(V)_3$ while the peak at around 1020 cm^{-1} is assigned to V=O stretching vibration.[25-27] After the hydrothermal reaction, the new bands at 1569 and 1610 cm^{-1} are corresponding to the characteristic C=C stretching mode of benzenoid and quinonoid rings, respectively while the bands located at 1304 and 1468 cm^{-1} are related to the C-N and C=N stretching vibration. [28, 29] Additionally, the new bands at 1133 and 1242 cm^{-1} are assigned to the C-H bendings of the quinonoid- and benzenoid-rings, respectively. The features suggest the formation of protonated polyaniline. The electronic conductivity of polyaniline is dependent on doping degrees and would further change the electrochemical performance. More importantly, the two typical bands at 495 and 621 cm^{-1} for stretching modes of V-O-V were merged into a broaden one centered at 534 cm^{-1} after the hydrothermal reaction, which could be contributed to the restricted stretching due to the presence of guest molecules between the layers. The shifting to the low band number of 1003 cm^{-1} for the V=O band suggests the formation of hydrogen bonding (N-H···O=V) between PANI and vanadyl groups. This was also confirmed by Raman spectra (Figure S3). These results suggest the successful intercalation of V_2O_5 with PANI.

According to the results of DSC/TGA (Figure S4), the weight loss (2.5%) below 150°C is mainly attributed to the physically absorbed water. Subsequently, one decalescence peak appears at around 287°C, corresponding to the loss of structure water (10.9%). A significant weight loss between 345-426°C can be contributed to the thermal decomposition of PANI in air.[30, 31] After the thermal treatment, although the annealed V_2O_5 exhibits similar nanoflakes with a larger thickness (Figure S5), the XRD diffraction peaks are indexed to the orthorhombic V_2O_5 (JCPDS 41-1426, Figure S6) without intercalation due to burning out of polyanilines. The

content of V element is determined to be 40.6 wt% by ICP-MS test, comparable to the TGA result (Table S1).The above results confirm the formation of PANI intercalated vanadium oxides with the molecular formula of $V_2O_5 \cdot 0.3C_6H_6N \cdot 1.5H_2O$.

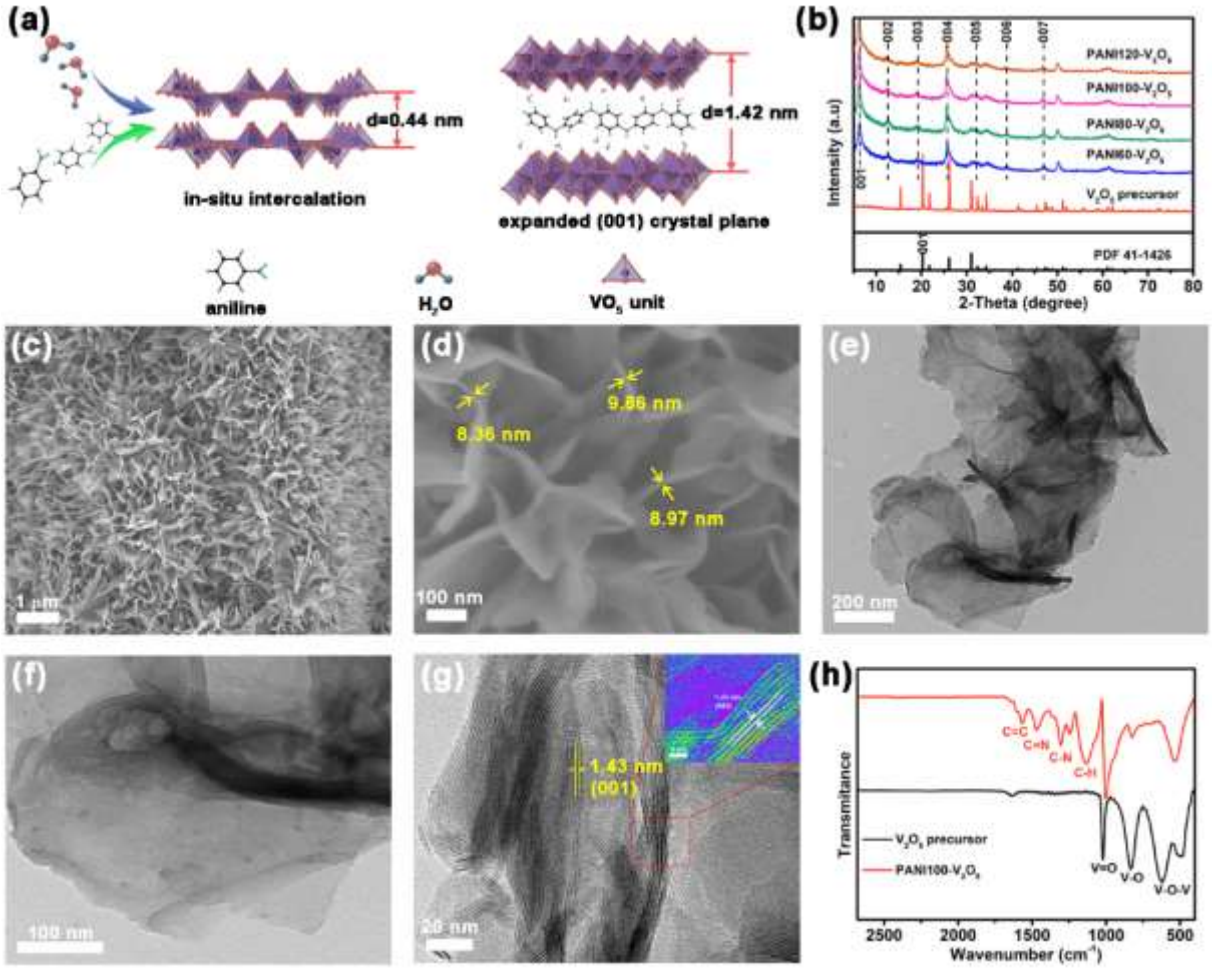

Figure 1. a) Schematic illustration for extending the interlaminar spacing of V_2O_5 via the intercalation with PANI. b) XRD pattern of V_2O_5 precursor and intercalated V_2O_5 with different amount of PANI. c, d) SEM images of PANI100-V_2O_5. e, f) TEM and g) HRTEM images of PANI100-V_2O_5. h) FTIR spectra of V_2O_5 precursor and PANI100-V_2O_5.

On the basis of the above observations, the interconnected nanosheets were formed along with gradually crystalline changes under the hydrothermal treatment. It was reported that the aniline monomers polymerized among the defined spaces of layered montmorillonite.[32] In contrast, the present case demonstrated that the polymerization of aniline monomers and gradual intercalations led to the formation of polyaniline intercalated vanadium oxide with

broadening interlayer space. Typically, the redox reaction between V_2O_5 and the aniline monomers under hydrothermal treatment is responsible for the in-situ intercalation of polyaniline, accounting for the partial reduction of vanadium oxide.

To further reveal the effect of polyaniline on the intercalation process of vanadium oxide, the amounts of aniline monomers was changed from 60 to 120 μL. As displayed in Figure S7, the V_2O_5 particles are aggregated covered with short nanosheets in the presence of aniline monomers (60 μL). With gradually increasing aniline monomers, the bulk material transforms into nanoflakes with a larger size and thinner thickness. With the addition of 100 μL aniline monomers, the final product shows uniform nanoflakes interconnected with each other. More importantly, the low-angle shift of (001) diffraction peaks with the increasing interlayer spacing can be contributed to the gradual intercalation of polyaniline with increasing aniline contents (Figure 1b). At the same time, the formation of polyaniline chains can also contribute to the preferable formation of the V_2O_5 nanosheets with a larger lattice spacing. Increasing the hydrothermal temperature to 160°C, XRD pattern suggests the formation of monoclinic VO_2 (JCPDS 81-2392, Figure S8) due to the further reduction. However, the nanoflakes were transformed into nanorods with diameters of tens to hundreds of nanometers (Figure S9). The results indicate a suitable temperature is favorable to the gradual intercalation of polyaniline among vanadium oxides.

The survey X-ray photoelectron spectroscopy (XPS, Figure S10) [31, 33] shows the existence of V, O, N, C elements. The core-level V $2p_{3/2}$ can be divided into two bands at 517.5 and 516.2 eV, corresponding to V^{5+} and V^{4+}, respectively. The presence of low valence with a V^{5+}/V^{4+} ratio of around 4.3 according to the peak area indicated the partial reduction of vanadium oxide during the polymerization of aniline. The bands located at 530.1 and 532.3 eV are corresponding to the O 1s in V_2O_5 and the adsorbed water in the interlayer, respectively. Importantly, the band situated at 399.9 eV can be fitted into three bands for the quinoid imine

(-N=, 399.2 eV), benzoid amine (-NH-, 400.1 eV) and positively charged nitrogen (-$N^{\cdot+}$-, 402.3 eV), respectively, confirming the formation of polyaniline.

2.2. Electrochemical performance

The electrochemical performances of samples were investigated in a two-electrode configuration by coupling with a polished zinc plate in 3 M $Zn(CF_3SO_3)_2$ electrolyte. As a comparison, the pure PANI nanofibers with the diameter of 20-30 nanometers (Figure S11) were synthesized according to an oxidized polymerization process. The XRD pattern with three diffraction peaks located at 9, 20 and 25° suggested the high crystallinity and proton doped characteristic of PANI (Figure S6).[34, 35] The CV curve in the Figure 2a exhibits a sharp oxidation peak at 1.10 V and a wide reduction peak at 0.76 V, that can be contributed to the redox process of polyaniline without obvious ion insertion/extraction feature. Similarly, the annealed V_2O_5 electrode also exhibits the non-featured CV curves at the given scan rate. Three pairs of non-obvious redox peaks at the low scan rate of 0.1 mV s^{-1} rapidly disappeared with increasing the sweeping rate (Figure S12). The results indicated that the slight insertion/extraction of zinc ions can be achieved at the annealed vanadium oxide electrode, but cannot at the polyaniline electrode due to the sluggish kinetic process and the large size of hydrous zinc ions. In contrast, the CV profiles of PANI100-V_2O_5 demonstrated three pairs of cathodic/anodic peaks at 0.70/0.48, 0.87/0.71 and 1.00/0.89 V. The well-defined peaks with good reversibility suggest the multi-step charge storage process, which is different with the simple insertion/extraction process of the reported ZIBs based on V_2O_5 cathodes.[17, 24, 36] The typical intercalation feature is expected to enhance specific capacity and accelerate the ion kinetics for high-rate performance.

To reveal the influence of polyaniline intercalation on the electrochemical performance of samples, various samples prepared by changing the amount of aniline monomers and hydrothermal temperature were also examined by using the cyclic voltammetry. Even in the presence of a small amount of aniline monomers (60 uL), the resultant sample exhibited the

enhanced intercalation feature of zinc ions with the obvious peaks in comparison with the pure vanadium oxide at a given scan rate (Figure S12b & S13a). With increasing the amount of aniline, the CV curves gradually exhibit three pairs of typical redox peaks and the PANI100-V_2O_5 electrode exhibits the largest curve area, corresponding to the largest specific capacity (Figure S13a-d). The peak potentials of each redox couple were measured to evaluate the reaction reversibility. The smaller potential difference suggests the lower polarization with improved reversibility. Accordingly, good reversibility can be achieved at the PANI100-V_2O_5 electrode (Figure S13e). These experimental results revealed that the intercalation of vanadium oxide with polyaniline gradually can extend the lattice spacing, and thus enhance the kinetic process for improving the electrochemical performance. However, the excessive aniline was polymerized on the surface of V_2O_5 (Figure S7), slowing down the kinetic process of electrode reaction. Moreover, excessive intercalation of polyaniline molecules can deteriorate the stability of the lattice structure, resulting in poor rate performance and cycling stability. Therefore, favorable electrochemical properties were achieved at the sample prepared in the presence of 100 μL aniline. The detailed electrochemical tests of assembled ZIBs (Figure S14) further revealed the optimized performance achieved by the appropriate intercalation with polyaniline.

The CV test was performed at 0.1 mV s^{-1} to evaluate the cycling stability of PANI100-V_2O_5 cathode. The obvious activation process is observed on the basis of the derivation of the first cycle of CV from the subsequent ones. The highly overlapped CV and galvanostatic charging/discharging curves (Figure 2b & S15) suggest good reversibility during the cycling test. The initial specific capacity was 348 mAh g^{-1} and improved up to 372 mAh g^{-1} via the activation process. As shown in Figure 2c, the specific capacities of PANI100-V_2O_5 cathode are around 360, 342, 318, 272, 236 and 216 mAh g^{-1}, respectively at increasing current density from 0.5, 1, 2, 5, 8 to 10 A g^{-1}. The specific capacity of the annealed vanadium oxides gradually increased to around 352 mAh g^{-1}, comparable to that of PANI100-V_2O_5. However, when the

current density was increased by 20 times, the capacity retention is around 60% for PANI100-V_2O_5, which is higher than those of PANI (50%) and the annealed vanadium oxide (5%). The results are in good agreement with that of CV measurements, highlighting the good high-rate performance of PANI-V_2O_5 possibly due to the extended interlaminar spacing. When the current density returned to 0.5 A g^{-1}, the reversible capacity of PANI100-V_2O_5 was 351 mAh g^{-1}, demonstrating the good reversibility and hence long-term cycling stability. Prior to evaluating the long-term cycling life, the ZIBs were firstly activated at 0.5 A g^{-1} for 10 cycles. The initial discharging capacity of 275 mAh g^{-1} at a current density of 5 A g^{-1} and maintained at 208 mAh g^{-1} after 2000 cycles. Impressively, the specific capacity and cycling stability of Zn//PANI100-V_2O_5 battery are superior to the vanadium-based aqueous rechargeable ZIBs reported recently (Table S2), demonstrating the great potential for next-generation energy storage.[7, 14, 23] In contrast, the capacity retention of the annealed V_2O_5 is only 53%. As no obvious intercalation feature of zinc-ion was observed at the PANI electrode, the redox process of PANI with the possible proton doping/de-doping process led to an acceptable capacity retention of around 90% over 2000 cycles (Figure 2e).

To elaborate on the relationship between crystal structure and electrochemical performance, the samples were prepared at the hydrothermal temperatures of 120 and 160 °C for comparison. Similar to that of the PANI100-V_2O_5 cathode, the CV profile PANI-V_2O_5-120 cathode exhibits three-pairs of redox peaks with good reversibility (Figure S16a). However, the specific capacity of 297, 276, 233, 199, 183 and 133 mAh g^{-1} at the current density of 0.5, 1, 2, 5, 8 and 10 A g^{-1}, respectively are relatively smaller than those of PANI100-V_2O_5 and the capacity retention is about 85% after 100 cycles, that is lower than that of PANI100-V_2O_5 (97%) (Figure S17a-c). The PANI-V_2O_5-160 electrode exhibited the distorted CV curves without obvious peaks (Figure S16b), suggesting the poor intercalation process. The galvanostatic charge-discharge tests also exhibited poor rate-performance (Figure S17d-f). The results demonstrated the electrochemical properties of as-prepared samples are highly dependent on the preparation process with the

polyaniline intercalation. At the low hydrothermal temperature of 120 °C, PANI was introduced into the vanadium oxide for improving the facile intercalation of zinc ions. However, the low crystallinity of PANI-V_2O_5-120 was not able to maintain the lamellar structures for long-life stability. In contrast, the formation of nanofibers with obviously small lattice spacing (Figure S9) suggested that PANI can not be intercalated into vanadium oxide at the higher temperature of 160 °C, resulting in much poor performance.

According to the electrochemical impedance spectra (EIS, Figure S18a), the smaller semicircle for the PANI100-V_2O_5 suggests the lower charge-transfer resistance in comparison with the pure PANI and the annealed V_2O_5. The mesoporous structure with the improved electronic conductivity of PANI via the doping allows the multiple ions accessible for improving electrochemical properties (Figure S19).[31] Especially, the quite small solution resistance can be ascribed to the superior wettability of the electrode materials in the electrolyte (Figure S20). These unique features obviously contribute to the favorable interaction process of PANI100-V_2O_5 electrode in the aqueous electrolyte of $Zn(CF_3SO_3)_2$ (Figure S21-22). Additionally, the charge transfer resistance is about 50 Ω initially, subsequently increased to 90 Ω at the 100th cycle, but no obvious increase is observed even after the 500th cycle. The results indicated the formation of a stable electrode-electrolyte interface without obvious structure change during the long-term cycling test (Figure S23). Meanwhile, thin nanoflakes without the formation Zn dendrites were observed at the surface of Zn anode after the continuous cycling test, which can also contribute to the improved cycling stability (Figure S24). Notably, the interaction of vanadium oxide can also be achieved by using polypyrrole on the basis of the same preparation process (Figure S25). However, the relatively poor battery performances were observed (Figure S26) in comparison with PANI100-V_2O_5 electrode, which can be contributed to the different molecular structure of polypyrrole. A deeper study is needed to understand the different performance in the future. Nevertheless, the present method provides a general

approach to enhance the performance of vanadium oxide via the pre-intercalation with conducting polymers.

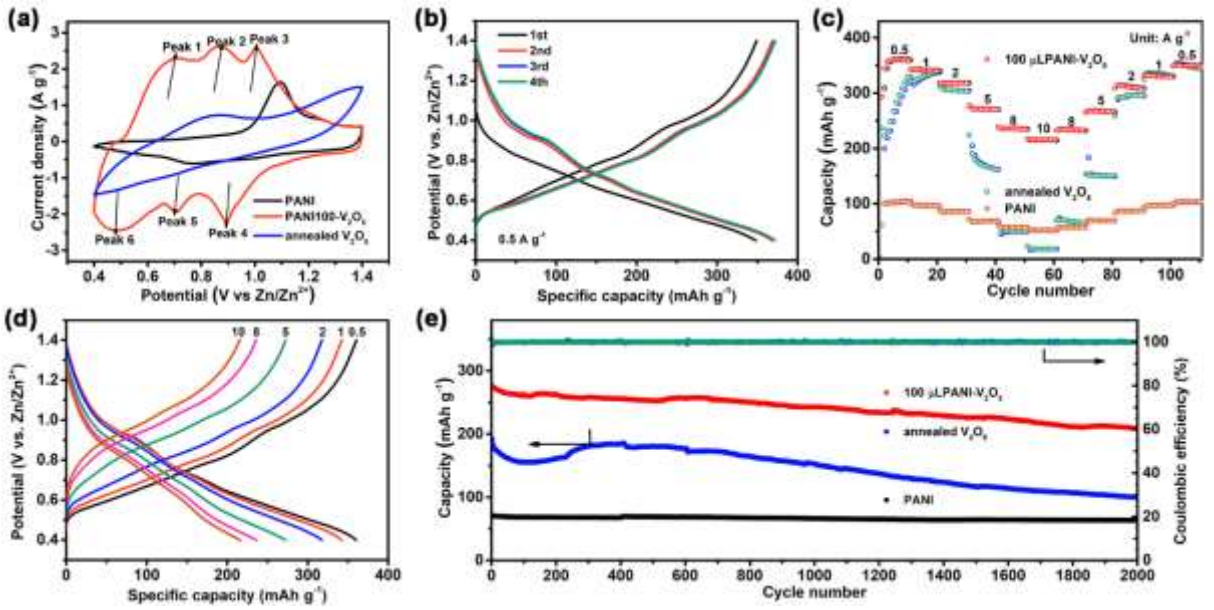

Figure 2. a) Cyclic voltammetry curves of PANI, PANI100-V_2O_5 and the annealed V_2O_5 electrode. b) Galvanostatic charge/discharge profiles of PANI100-V_2O_5 at 0.5 A g^{-1}. c) Rate performance and d) the corresponding charge/discharge curves of PANI100-V_2O_5 at various current densities. e) Cycling performance of PANI, PANI100-V_2O_5 and annealed V_2O_5 at 5 A g^{-1} for 2000 cycles.

To gain deeper insight into the electrochemical kinetics of polyaniline chelated vanadium oxide electrode, the cyclic voltammetry (CV) measurement was carried at the scan rate range of 0.1 to 1 mV s^{-1} (Figure 3a). Three pairs of highly symmetrical redox peaks with a slight potential shift with increasing scan rates suggest the highly reversible redox reactions. The qualitative description of electrode reaction process is established according to the proposed relationship between current (i) and scan rate (v):

$$i = av^b \quad (1)$$

where a and b are adjustable parameters. The b values of six peaks were calculated to be 0.84, 0.94, 1.01, 0.86, 0.88 and 0.91 (Figure 3b), suggesting the dominant surface controlled behavior.[37, 38] Considering the hybrid composition and intercalation structure of the present

electrode material, the contribution of surface capacitance is determined according to equation (2):

$$i = k_1 v + k_2 v^{1/2} \quad (2)$$

where $k_1 v$ and $k_2 v^{1/2}$ represent the current contribution from surface capacitance and diffusion-controlled faradic process, respectively. The contribution ratio of surface capacitance was calculated to be 71.9, 75.9, 80.5, 84.9, 88.3 and 88.9% at the scan rate of 0.1, 0.3, 0.5, 0.7, 0.9 and 1 mV s^{-1}, respectively (Figure 3c & Figure S27). Different from the bulk materials, the energy storage process of PANI100-V_2O_5 electrode is dominated by the surface capacitance due to the thin nanoflake structure with abundant mesopores (Figure S19), which can contribute to the high-rate performance and stability for Zn-ion storage. The galvanostatic intermittent titration technique (GITT) technique was performed to determine the Zn^{2+} ion diffusion coefficient (D, cm^2 s^{-1}) of the PANI100-V_2O_5 cathode (Figure 3d). On the basis of the enlarged galvanostatic charge/discharge curves (Figure 3e & S28), the D values calculated are in the range of $1.5 \sim 4.3 \times 10^{-7}$ and $1.0 \sim 3.4 \times 10^{-7}$ cm^2 s^{-1} during the charge and discharge process, respectively, which are higher than those of the reported materials for ZIBs (Table S3).[33, 36] The larger diffusion coefficient highlights the unique features of composite electrode for favorable zinc ion diffusion. It has been revealed that the structural water molecules act as a shielding layer can effectively weaken the electrostatic interaction between zinc ion and lattice oxygen, thus enhancing the diffusion coefficient of zinc ions. [39] In the present case, the PANI plays the crucial role in enlarging the lattice spacing (1.42 nm) of vanadium oxide in addition to the small amount of water. The large spacing would provide favorable channels for the rapid Zn^{2+} diffusion. Additionally, the charges and electrons are able to be shared among the polyaniline chains via the π-π conjugated structure.[40] Therefore, the polyaniline chain as flexible pillar would facilitate the rapid transport of zinc ion along with doping/de-doping process, resulting in the larger diffusion coefficient of zinc ion. It suggests the favorable kinetic

process of electrode materials for zinc ion storage, leading to good high-rate performance. Furthermore, the negligible differences in the diffusion coefficient between the charge and discharge process (Figure 3f) show the good reversibility of zinc ions insertion and extraction process.

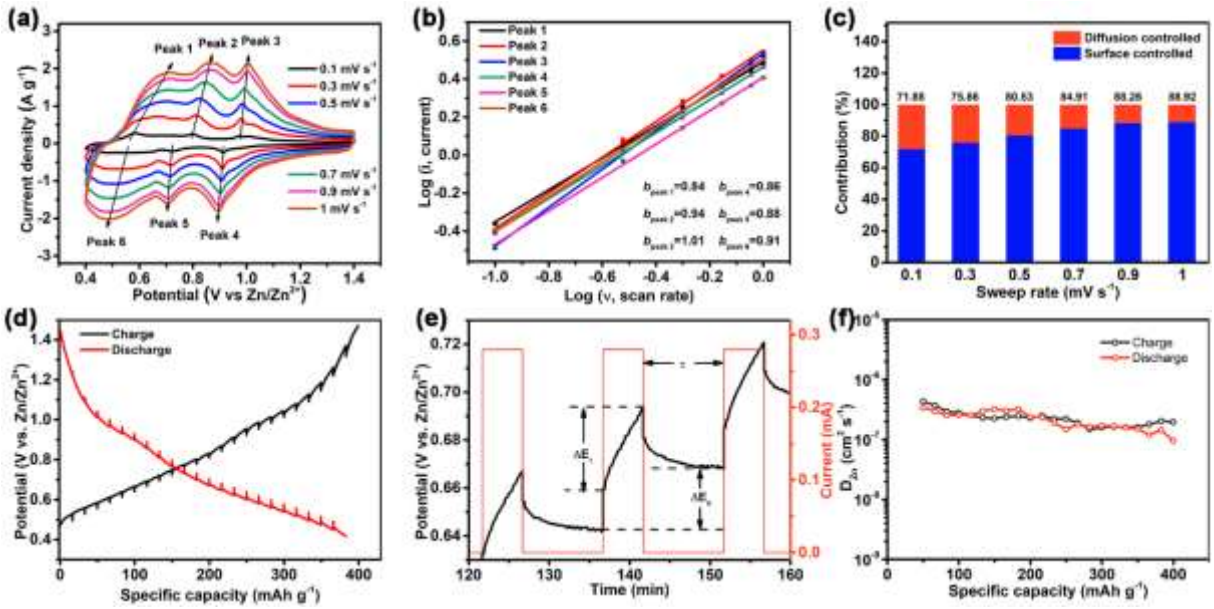

Figure 3. a) CV curves of PANI100-V_2O_5 at various scan rates. b) The linear fitting curves of log *i* versus log ν according to the CV results in (a). c) Diffusion-controlled and surface controlled contributions to capacity at various scan rates. d) Galvanostatic intermittent titration technique (GITT) curves at the current density of 0.2 A g^{-1} and the selected steps e) during the charging process. ΔE_s and ΔE_t are corresponding to the steady-state potential change by the current pulse and the voltage change during the constant current pulse, respectively. f) The corresponding Zn^{2+} diffusion coefficient at various states of charging and discharging process.

2.3. Mechanism discussion

To investigate the underlying energy storage mechanism along with the structural evolution of PANI intercalated vanadium oxide, in-situ XRD measurements were performed during the charging/discharging process. As demonstrated in Figure 4a & b, the XRD patterns revealed that the crystal structure of PANI100-V_2O_5 is fully reversible during the intercalation and extraction of Zn^{2+} ions. Upon discharging process, the peaks of (00*l*) lattice planes shifted to

small angles owing to the intercalation of Zn^{2+} ions. At the end of the first discharge platform located at 0.82 V, around 0.36 mol of Zn^{2+} ions is intercalated into the interlayer of PANI100-V_2O_5 electrode ($V_2O_5{\cdot}0.3C_6H_6N{\cdot}1.5H_2O$) according to the specific capacity tested. With the increasing amount of intercalated Zn^{2+} ions, new diffraction peaks observed at 5.5, 11.1, 16.6° suggest the interlayer spacing is enlarged to around 1.62 nm. It has been reported that the irreversible structure transition, including the phase transformation, is due to the lattice volume expansion, resulting in poor stability of electrode materials.[41, 42] In the present case, the expansion of pristine phase was calculated according to the slight peak shift from 25.1 to 24.5° for the (004) lattice plane, which is corresponding to the interplanar distance extended from 0.35 to 0.36 nm. The similar lattice variations were also detected at 44.8 and 58.4° for the (007) and (009) lattice planes, respectively. The negligible spacing change is more favourable to maintain the stability of the bulk structure. More importantly, the accumulation of more Zn^{2+} ions can be achieved via the smoothly enlarging interlayer spacing from 1.42 to 1.62 nm, as calculated from the variation of diffraction peaks (Figure 4c), leading to the larger specific capacity. Upon the charging process to 1.4 V, the (00*l*) peaks of pristine phase gradually returned to the initial state, and no additional impurity was observed during the whole cycling process, further suggesting the good structure reversibility.[15] To demonstrate the superior features of $V_2O_5{\cdot}0.3C_6H_6N{\cdot}1.5H_2O$, the structure changes of the annealed sample without polyaniline guest material was also detected by using the in-situ XRD method (Figure S29). The initial diffraction peaks matched well with the orthorhombic V_2O_5 (JCPDS 41-1426). For the discharging process, the peaks of crystal faces (200), (001), (301), (011), (310), (002) and (411) disappeared with the intercalation of Zn^{2+} ions. The large structure changes for the accumulation of Zn^{2+} ions was due to the narrow ion channels, resulting in low capacity and poor reversibility. It is evidenced that the intercalated amount of Zn^{2+} ions was calculated to be 0.25 mol, that is less than that of $V_2O_5{\cdot}0.3C_6H_6N{\cdot}1.5H_2O$ (0.36 mol). Therefore, the polyaniline

intercalated V_2O_5 with larger interlaminar spacing is able to provide enough space for accumulating additional Zn^{2+} ions. The conjugated PANI chains as interlayer pillars would provide the structure flexibility in the confined space to reversibly buffer the layer spacing expansion. It has been revealed that the precise synthesis of the vanadium oxide nanostructures with specific crystal planes is crucial to provide open interlayers for facile sodium ion intercalation.[43, 44] In contrast, the present work demonstrated that PANI is favorable to regulate the lamellar structure of vanadium oxide with the flexible organic pillar for enhancing the specific capacity and also effectively buffering volume changes for the good cycling stability. The plausible charge storage process (Figure 4c) demonstrates that the reversible intercalation of zinc ions at the PANI100-V_2O_5 electrode with the stable (001) crystalline structure avoids the phase transformation for improving cycling stability.

To further elucidate the energy storage process, X-ray photoelectron spectroscopy (XPS) was conducted to examine the various statuses of the PANI100-V_2O_5 electrode for the charging/discharging process. As shown in figure 5a, C, N, V, O, F, Zn elements are detected in discharged (0.4 V) and charged states (1.4 V). The initial V $2p_{3/2}$ signal can be split into two peaks at 517.6 and 516.3 eV, corresponding to the V^{5+} and V^{4+}, respectively (Figure 5b).[45, 46]. However, no Zn element is found in the initial state (Figure 5c). For the preparation of the PANI intercalated V_2O_5 in the acidic solution, the formation of protonated polyaniline is responsible for complementing the electronic conductivity via the doping process. Specifically, the N 1s signal (Figure 5d) is deconvoluted into three peaks, corresponding to the quinoid imine (-N=, 399.4 eV), benzoid amine (-NH-, 400.2 eV) and positively charged nitrogen (-N^+-, 401.4 eV), respectively.[31] Polyaniline has been used as capacitive materials via the quinone redox mechanism with the reversible doping/de-doping process.[47, 48] The polymeric chains could be broken due to the prolonged redox process, resulting in the poor cycling stability of polyaniline. In the present case, both Zn^{2+} ions and proton were involved in the charge storage process of

polyaniline. In the confined space of the lamellar vanadium oxide, the redox degradation could be eliminated along with the reversible doping process of multiple ions (e.g., H^+, Zn^{2+}).

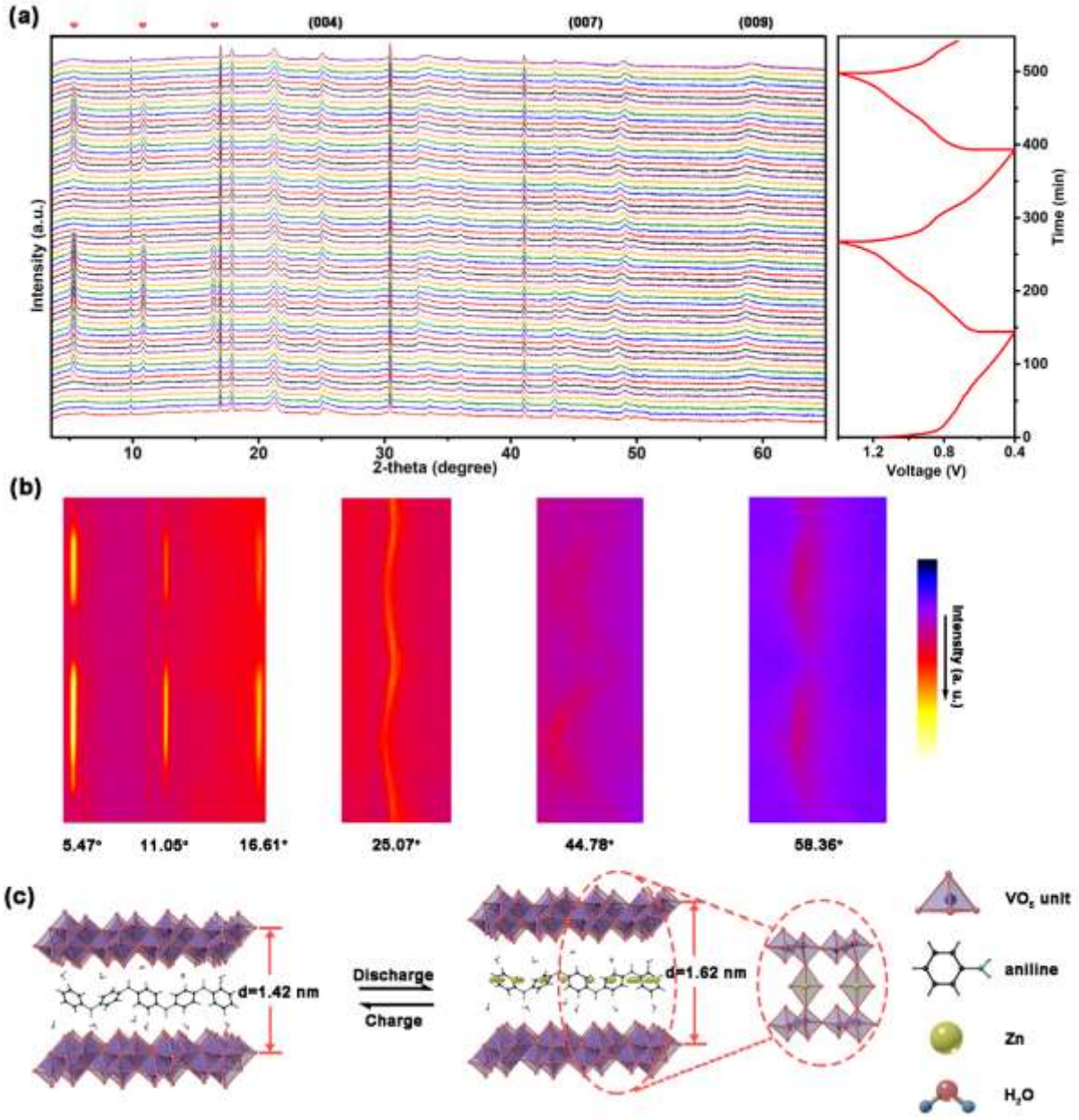

Figure 4. a) In-situ XRD test and the corresponding time-voltage curve. b) The corresponding high-resolution contour maps. c) Schematic illustrations of zinc ion insertion/extraction of PANI100-V_2O_5 during the discharging/charging process.

In the initial discharged state, the proportion of V^{5+} decreases from 81 to 21%, with an emerging peak at 515.6 eV assigned to the V^{3+} (Figure 5b) that is due to the reduction of vanadium oxide. The Zn $2p_{2/3}$ signals at 1023.8 and 1022.8 eV are corresponding to the

intercalated Zn^{2+} ions among the interlayers of V_2O_5 and the absorbed Zn^{2+} ions on the surface of PANI100-V_2O_5 electrode, respectively.[33] Remarkably, with the reduction of quinone imine (~26%) the positively charged nitrogen was increased from 31 to 47% because of the combination with Zn^{2+} and/or H^+ ions. When further charged to 1.4 V, the peak area ratio of V^{5+}/V^{4+} almost recovers to the initial value of 4.3 (Figure 5b). The weak peak of Zn 2p in the charged state can be ascribed to the residual Zn^{2+} ions absorbed on the surface of PANI100-V_2O_5. Meanwhile, the benzoid amine (~53%) was oxidized to quinone imine (~78%), and the positively charged nitrogen was reduced to 19%, that is due to the removal of Zn^{2+} and/or H^+ ions.

It was reported that the insertion of both Zn^{2+} and H^+ simultaneously can enhance the specific capacity of manganese oxide.[9, 49] However, the stability of the materials was deteriorated owing to degradations at high concentrations of H^+ ions in the confined space. The issue can be well-addressed via the doping process of polyaniline, that intercalated among the layers of vanadium oxide. The in-situ ATR FTIR was employed to investigate the changes in the characteristics of functional groups during the operation of ZIB (Figure 5e & S30). In the initial stage, the characteristic bands of polyaniline located at 1596, 1499 and 1300 cm^{-1} are corresponding to the C=C, C=N stretching vibration of the quinoid ring and C-N stretching mode of the benzoid ring, respectively,[25] in addition to the C-F asymmetric stretching vibration of PTFE as the binder (around 1203 cm^{-1}). Notably, in the discharge process, it can be seen that the band at 1596 cm^{-1} for the quinoid ring is gradually declined and the C=N stretching vibration at 1499 cm^{-1} weakens whereas a new band at 1544 cm^{-1} is growing bigger and bigger, which is corresponding to the C=C stretching vibration in the benzoid ring. The results suggested the reduction of the quinoid ring into the benzoid ring. In contrast, the gradually increasing band of C-N stretching mode and the redshift are caused by the protonation induced π-electron delocalization among the polyaniline chain during the discharging process.[50] During the recharge process, the characteristic bands of the benzoid ring gradually disappeared, that is due

to the oxidation process along with the intercalation of Zn^{2+} and/or H^+ ions. Especially, the formation of the bipolaron structure can improve the conductivity of the electrode material.[51] More importantly, the intensity and position of various bands returned to the initial state (Figure 5e), suggesting the good reversibility of PANI100-V_2O_5 cathode.

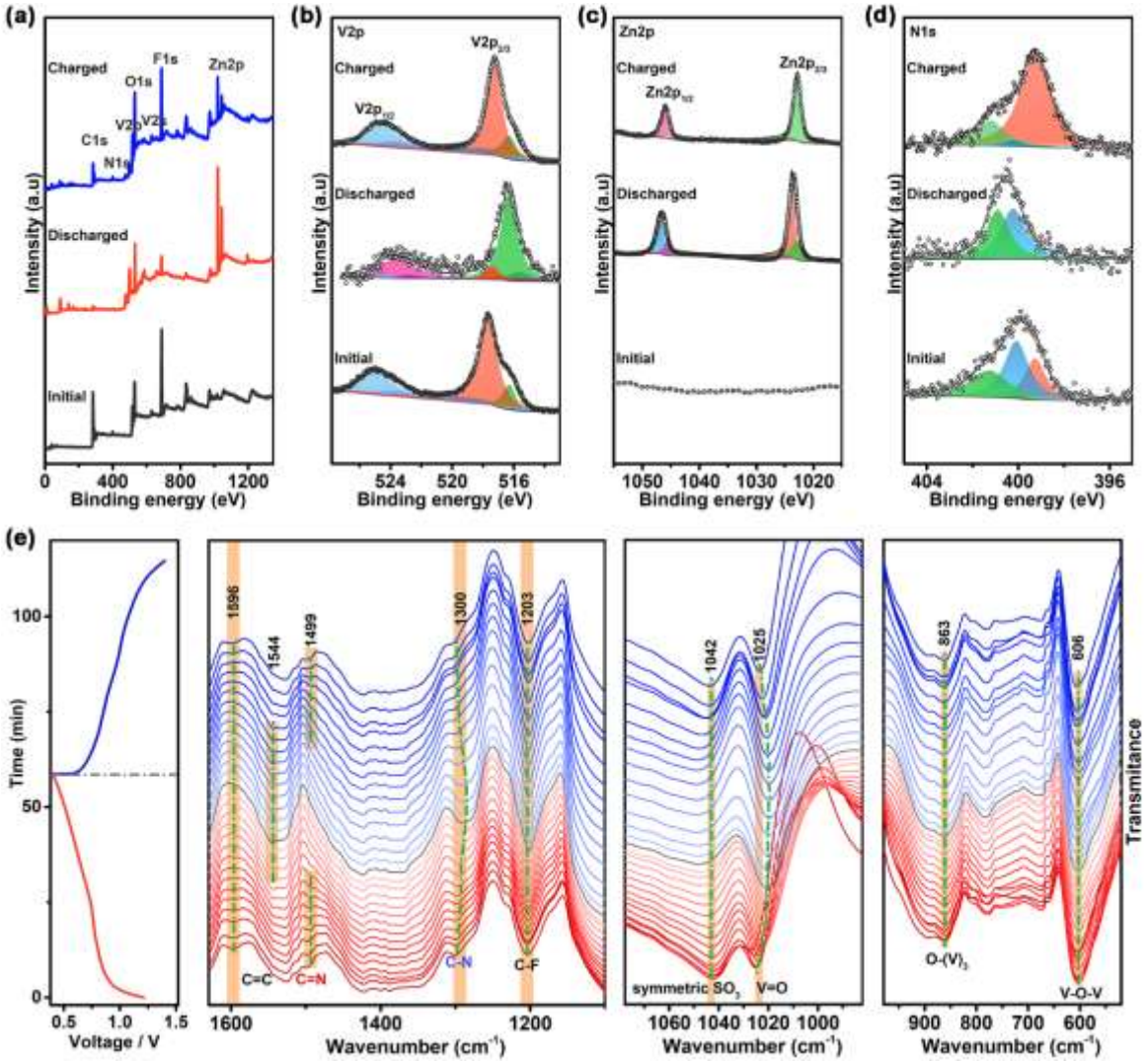

Figure 5. a) Survey XPS spectra and high-resolution XPS spectra of b) V 2p, c) Zn 2p, d) N 1s at initial, discharged and charged states. e) In-situ ATR FTIR spectra of PANI100-V_2O_5 in the first cycle.

The previous work revealed that $CF_3SO_3^-$ ion from the electrolyte is involved in the charging process accounting for the charge balance, causing serious volume expansion because of the large size. [19] In the present work, the bands located at 1042 cm^{-1} are assigned to symmetry stretching vibration of SO_3 in $CF_3SO_3^-$.[52, 53] During charge and discharge process, no obvious

band change is observed, demonstrating that $CF_3SO_3^-$ is not involved in the whole energy storage process. Along with V=O stretching vibration at 1025 cm^{-1}, the bands located at 863 and 606 cm^{-1} are corresponding to the vibration of $O\text{-}(V)_3$ and stretching modes of V-O-V, respectively. Upon the discharge process, the redshift of the V=O stretching vibration to 1020 cm^{-1} can be attributed to the intercalation of zinc ions that attract oxygen atoms and weaken the V=O bond because the terminal V=O stretching vibration is more sensitive towards the crystalline variation.[54] Upon the charging process, the band location of V=O stretching vibration returns to the original position, suggesting the good reversibility of PANI intercalated vanadium oxide without serious volume expansion. Previously, the step-by-step intercalation mechanism of Zn^{2+} and H^+ ions has been proposed to understand the improved performance of manganese dioxide-based electrode materials.[9] Notably, the pH value of the electrolyte solution was tested during the charging and discharging process (Figure 31). The slightly increased pH value of electrolyte during the discharging process would be attributed to the gradual intercalation of H^+ ions into the interlayers of V_2O_5 via the doping process of polyaniline. In contrast, upon the charging process, the pH of electrolyte solution gradually decreases along with the de-doping process of polyaniline. The present results demonstrate that the pre-intercalation of vanadium oxide with PANI enables the reversible intercalations of zinc and/or H^+ ions by the combination of conducting polymers and the layered vanadium oxide. Therefore, The pre-intercalation of polyaniline with the conjugated structure not only enlarges the lattice spacing of vanadium oxide for reversibly accumulating zinc ions, but also contributes to the charge storage process via the doping process and conversion reactions. Especially, the conducting polymer can act as a interlayer pillar and shielding layer in the organic-inorganic hybrid material to improve the energy storage process, leading to the enhanced electrochemical performance.

3. Conclusion

In summary, we have successfully synthesized PANI intercalated V_2O_5 through the one-pot hydrothermal method. The in-situ intercalation of PANI in V_2O_5 enables the optimization of the interlaminar structure of hybrid electrode materials by adjusting the temperature and the ratio of aniline to V_2O_5. The resultant PANI intercalated V_2O_5 with enlarged layer spacing demonstrated larger specific capacity and superior rate performance than that of the pristine orthorhombic V_2O_5. Polyaniline as a pillar also endows the composite good cycle stability. More importantly, findings from the in-situ XRD and in-situ IR studies revealed that the polyaniline as the guest materials not only enlarges the lattice spacing for easily accumulating Zn^{2+} ions to improve the specific capacity, but also buffers the structural expansion due to the flexible molecular nature for improving the stability. Additionally, the reversible doping process of polyaniline enables the multiple ions of Zn^{2+} and H^+ involved in the charge storage process, leading to improved battery performance via the synergistic effect. Uncovering the origin of improved charge storage mechanism provides basic principles to rationally design organic-inorganic hybrid materials for enhancing zinc ion storage.

4. Experimental Section

4.1. Material preparation

In a typical procedure, 0.18 g of V_2O_5 was dispersed into 30 mL ultrapure water under vigorous stirring, and a given amount of aniline was added subsequently. Then, the pH of the solution was adjusted to about 3 by adding appropriate hydrochloric acid. The resulting mixture was transferred into a 50 mL Teflon-lined autoclave and maintained at 140°C for 24 h. After that, the collected precipitation was washed with ultrapure water and dried at 60°C for 8 h in a vacuum oven. To examine the intercalation process, the amount of aniline monomers was changed from 60 to 120 uL and the resultant samples were named as PANI60-V_2O_5, PANI80-V_2O_5, PANI100-V_2O_5, PANI120-V_2O_5, respectively. For comparison, the samples were also prepared by the same hydrothermal method at 120 and 160°C with the addition of 100 uL

aniline monomers, respectively, and named as PANI-V_2O_5-120 and PANI-V_2O_5-160. The sample was also synthesized by replacing aniline with pyrrole monomer and names as PPY100-V_2O_5. The control sample was also prepared by the same hydrothermal method without the addition of aniline monomers and denoted as HY-V_2O_5. Additionally, pure polyaniline was also synthesized. 0.3 mL aniline and 0.18 g $(NH_4)_2S_2O_8$ was dissolved in 10 mL HCl solution (1 mol L^{-1}), respectively. The two solutions were mixed together under strong stirring, then kept in an ice bath for 2 h. The resulting precipitation was collected and washed with deionic water for three times, and dried at 60°C for 8 h in a vacuum oven.

4.2. Material Characterization

The morphologies of samples were characterized by scanning electron microscopy (SEM, Gemini SEM 300, Carl Zeiss Microscopy GmbH). The crystallographic phases of samples and in-situ XRD data were collected using a Rigaku Dmax X-ray diffractometer with Ni-filtered Cu Kα irradiation. High-resolution transmission electron microscopy (HR-TEM, JEM-2100F) was conducted for further investigation of structure information. Raman spectra were carried out on a confocal laser Raman spectrometer (LabRAM HR800, HORLBA JY) under laser excitation at 633 nm. XPS measurement was conducted with a photoelectron spectrometer (ESCALAB 250). In-situ IR spectra were collected on the Bruker spectrometer with a home-made electrochemical cell. ICP-MS (NexION 350X) was used to determine the content of V element in sample.

4.3. Electrochemical Characterization

The electrode was prepared by mixing the active materials, acetylene black and Poly(vinylidene fluoride) (PVDF) with the mass ratio of 7:2:1. The resultant slurry was cast onto the stainless steel mesh and dried at 60°C for 8 h in a vacuum oven. The CR2016 coin-type cell was assembled by coupling with a zinc plate in 3 M $Zn(CF_3SO_3)_2$ electrolyte with a glass fiber separator. The cyclic voltammetry (CV) was performed on a CHI 760E

electrochemical workstation. The electrochemical impedance spectroscopy (EIS) was tested in a Gamry electrochemical workstation (USA) in the frequency range of 100 K Hz to 10 m Hz with AC amplitude of 10 mV. The galvanostatic charge–discharge was carried out with a Neware Battery Test System. The area loading of composite for each electrode is about 2.0~2.5 mg cm^{-2}, except that for in-situ XRD and in-situ IR test is ~23 mg cm^{-2}.

Supporting Information ((delete if not applicable))
Supporting Information is available from the Wiley Online Library or from the author.

Acknowledgements
This work was financially supported by the Taishan Scholars Program of Shandong Province (No. tsqn20161004), Program for Scientific Research Innovation Team of Young Scholar in Colleges and Universities of Shandong Province (2019KJC025) and the Youth 1000 Talent Program of China. The authors also acknowledge the assistance of the Analytical Center for Structural Constituent and Physical Property of Core Facilities Sharing Platform, Shandong University.

Received: ((will be filled in by the editorial staff))
Revised: ((will be filled in by the editorial staff))
Published online: ((will be filled in by the editorial staff))

References

[1] N. Balke, S. Jesse, A. N. Morozovska, E. Eliseev, D. W. Chung, Y. Kim, L. Adamczyk, R. E. Garcia, N. Dudney, S. V. Kalinin, *Nat. Nanotechnol.* **2010**, *5*, 749.

[2] K. Li, Z. Hu, J. Ma, S. Chen, D. Mu, J. Zhang, *Adv. Mater.* **2019**, *31*, e1902399.

[3] J. Ma, J. Sung, J. Hong, S. Chae, N. Kim, S. H. Choi, G. Nam, Y. Son, S. Y. Kim, M. Ko, J. Cho, *Nat. Commun.* **2019**, *10*, 475.

[4] J. Zhang, Z. Zhao, Z. Xia, L. Dai, *Nat. Nanotechnol.* **2015**, *10*, 444.

[5] N. Zhang, F. Cheng, Y. Liu, Q. Zhao, K. Lei, C. Chen, X. Liu, J. Chen, *J. Am. Chem. Soc.* **2016**, *138*, 12894.

[6] F. Wang, O. Borodin, T. Gao, X. Fan, W. Sun, F. Han, A. Faraone, J. A. Dura, K. Xu, C. Wang, *Nat. Mater.* **2018**, *17*, 543.

[7] Q. Yang, F. Mo, Z. Liu, L. Ma, X. Li, D. Fang, S. Chen, S. Zhang, C. Zhi, *Adv. Mater.* **2019**, *31*, e1901521.

[8] G. Fang, J. Zhou, A. Pan, S. Liang, *ACS Energy Lett.* **2018**, *3*, 2480.

[9] J. Huang, Z. Wang, M. Hou, X. Dong, Y. Liu, Y. Wang, Y. Xia, *Nat. Commun.* **2018**, *9*, 2906.

[10] H. Pan, Y. Shao, P. Yan, Y. Cheng, K. S. Han, Z. Nie, C. Wang, J. Yang, X. Li, P. Bhattacharya, K. T. Mueller, J. Liu, *Nat. Energy* **2016**, *1*, 16039.

[11] T. H. Shoji, M.; Yamamoto, T, *J. Appl. Electrochem.* **1988**, *18*, 521.

[12] B. Tang, L. Shan, S. Liang, J. Zhou, *Energy Environ. Sci.* **2019**, *12*, 3288.

[13] F. Wan, Z. Niu, *Angew. Chem. Int. Ed.* **2019**, *58*, 16358.

[14] M. Li, Q. He, Z. Li, Q. Li, Y. Zhang, J. Meng, X. Liu, S. Li, B. Wu, L. Chen, Z. Liu, W. Luo, C. Han, L. Mai, *Adv. Energy Mater.* **2019**, *9*, 1901469.

[15] D. Kundu, B. D. Adams, V. Duffort, S. H. Vajargah, L. F. Nazar, *Nat. Energy* **2016**, *1*, 16119.

[16] Z. Chen, V. Augustyn, J. Wen, Y. Zhang, M. Shen, B. Dunn, Y. Lu, *Adv. Mater.* **2011**, *23*, 791.

[17] J. S. Park, J. H. Jo, Y. Aniskevich, A. Bakavets, G. Ragoisha, E. Streltsov, J. Kim, S. T. Myung, *Chem. Mater.* **2018**, *30*, 6777.

[18] F. Wan, L. Zhang, X. Dai, X. Wang, Z. Niu, J. Chen, *Nat. Commun.* **2018**, *9*, 1656.

[19] F. Wan, L. Zhang, X. Wang, S. Bi, Z. Niu, J. Chen, *Adv. Funct. Mater.* **2018**, *28*, 1804975.

[20] V. P. Valeri Petkov, Pantelis Trikalitis, Christos Malliakas,, M. G. K. Tom Vogt, *J. Am. Chem. Soc.* **2005**, *127*, 8805.

[21] E. R. Z. F. Li, *Langmuir* **2002**, *18*, 6956.

[22] L. Shan, Y. Yang, W. Zhang, H. Chen, G. Fang, J. Zhou, S. Liang, *Energy Storage Mater.* **2019**, *18*, 10.

[23] B. Sambandam, V. Soundharrajan, S. Kim, M. H. Alfaruqi, J. Jo, S. Kim, V. Mathew, Y.-k. Sun, J. Kim, *J. Mater. Chem. A* **2018**, *6*, 3850.

[24] M. Yan, P. He, Y. Chen, S. Wang, Q. Wei, K. Zhao, X. Xu, Q. An, Y. Shuang, Y. Shao, K. T. Mueller, L. Mai, J. Liu, J. Yang, *Adv. Mater.* **2018**, *30*, 1703725.

[25] R. M. Prakash R. Somani, A.B. Mandale, *Polymer* **2001**, *42*, 2991.

[26] Z. F. Y. Li Li, *Studies in Surface Science and Catalysis* **2005**, *156*, 523.

[27] Y. Zhang, *Materials Science-Poland* **2017**, *35*, 188.

[28] H. P. Cong, X. C. Ren, P. Wang, S. H. Yu, *Energy Environ. Sci.* **2013**, *6*, 1185.

[29] K. Li, X. Liu, S. Chen, W. Pan, J. Zhang, *Journal of Energy Chemistry* **2019**, *32*, 166.

[30] I. Karatchevtseva, Z. Zhang, J. Hanna, V. Luca, *Chem. Mater.* **2006**, *18*, 4908.

[31] K. Zhang, N. Li, X. Ma, Y. Wang, J. Zhao, L. Qiang, X. Li, Y. Li, *Journal of Electroanalytical Chemistry* **2018**, *825*, 16.

[32] W. Ding, Z. Wei, S. Chen, X. Qi, T. Yang, J. Hu, D. Wang, L. J. Wan, S. F. Alvi, L. Li, *Angew. Chem. Int. Ed.* **2013**, *52*, 11755.

[33] N. Zhang, M. Jia, Y. Dong, Y. Wang, J. Xu, Y. Liu, L. Jiao, F. Cheng, *Adv. Funct. Mater.* **2019**, *29*, 1807331.

[34] K. Lee, S. Cho, S. H. Park, A. J. Heeger, C. W. Lee, S. H. Lee, *Nature* **2006**, *441*, 65.

[35] A. Rahy, D. J. Yang, *Materials Letters* **2008**, *62*, 4311.

[36] Y. Yang, Y. Tang, G. Fang, L. Shan, J. Guo, W. Zhang, C. Wang, L. Wang, J. Zhou, S. Liang, *Energy Environ. Sci.* **2018**, *11*, 3157.

[37] T. Brezesinski, J. Wang, S. H. Tolbert, B. Dunn, *Nat. Mater.* **2010**, *9*, 146.

[38] V. Augustyn, P. Simon, B. Dunn, *Energy Environ. Sci.* **2014**, *7*, 1597.

[39] J. Shin, D. S. Choi, H. J. Lee, Y. Jung, J. W. Choi, *Adv. Energy Mater.* **2019**, *9*, 1900083.

[40] C. Hu, S. Chen, Y. Wang, X. Peng, W. Zhang, J. Chen, *J. Power Sources* **2016**, *321*, 94.

[41] T. M. Jin Kawakita, Tomiya Kishi, *J. Power Sources* **1999**, *83*, 79.

[42] P. Gibot, M. Casas-Cabanas, L. Laffont, S. Levasseur, P. Carlach, S. Hamelet, J. M. Tarascon, C. Masquelier, *Nat. Mater.* **2008**, *7*, 741.

[43] D. Su, G. Wang, *ACS Nano* **2013**, *7*, 11218.

[44] D. Su, S. Dou, G. Wang, *ChemSusChem* **2015**, *8*, 2877.

[45] S. Kundu, B. Satpati, T. Kar, S. K. Pradhan, *J. Hazard. Mater.* **2017**, *339*, 161.

[46] Q. Pang, C. Sun, Y. Yu, K. Zhao, Z. Zhang, P. M. Voyles, G. Chen, Y. Wei, X. Wang, *Adv. Energy Mater.* **2018**, *8*, 1800144.

[47] J. Zhang, X. S. Zhao, *The Journal of Physical Chemistry C* **2012**, *116*, 5420.

[48] J. D. Andy Rudge, Ian Raistrick, Shimshon Gottesfeld, *J. Power Sources* **1994**, *47*, 89.

[49] W. Sun, F. Wang, S. Hou, C. Yang, X. Fan, Z. Ma, T. Gao, F. Han, R. Hu, M. Zhu, C. Wang, *J. Am. Chem. Soc.* **2017**, *139*, 9775.

[50] G. E. N. Zhao Ping, Helmut Neugebauer, Johannes Theiner, Adolf Neckel, *J. Chem. Soc., Faraday Trans.* **1997**, *93*, 121.

[51] M. C. Bernard, A. Hugot-Le Goff, *Electrochim. Acta* **2006**, *52*, 595.

[52] Moulay El Mustapha Hamidi, J. L. Pascal, *Polyhedron* **1994**, *13*, 1787.

[53] R. Rathika, O. Padmaraj, S. A. Suthanthiraraj, *Ionics* **2017**, *24*, 243.

[54] B. O. Angela Sˇ urca, *Electrochim. Acta* **1999**, *44*, 3051.

Pre-intercalation of V_2O_5 with polyaniline enables the regulation on the lamellar structure to accumulate reversibly zinc ions for improving the specific capacity and cycling stability of the aqueous zinc-ion battery.

Regulation on Lamellar Structure of Vanadium Oxide via Polyaniline Intercalation for High-Performance Aqueous Zinc-ion Battery

*Song Chen, Kang Li, Kwan San Hui and Jintao Zhang**

Keywords: aqueous zinc-ion battery; organic-inorganic material; intercalation; polyaniline; in-situ characterization

ToC figure